Chapter

Investigation of Structural, Microstructural, Dielectrical and Magnetic Properties of Bi3+ Doped Manganese Spinel Ferrite Nanoparticles for Photonic Applications

V. Jagadeesha Angadi, H.R. Lakshmiprasanna and K. Manjunatha

Abstract

The structural, microstructural, and magnetic properties of $Mn_{1-x}Bi_xFe_2O_4$ (where x = 0.0, 0.05, 0.1, 0.15, and 0.2) nanoparticles prepared by solution combustion method were investigated. Rietveld-refined X-ray diffraction patterns confirm the single-phase formation with space group Fd3m having spinel cubic structure. The porous nature of the samples was confirmed by scanning electron microscopy (SEM). Composition values of the theoretical stoichiometry and energy-dispersive spectroscopy (EDS) composition values are well matched for all samples. The dielectric parameters such as real part of dielectric constant, imaginary part of dielectric constant, and dielectric loss tangent decrease with the increase in frequency. The AC conductivity increases with increase in the Bi^{3+} concentration. The real part of complex impedance decreases with the increase in frequency. Cole-Cole plots reveal that one semicircle was obtained for each of the samples. The real and imaginary parts of electric modulus vary with frequency. The magnetic hysteresis curves of all samples reveal the soft magnetic material nature. We observed S esteems began uniquely from the higher superparamagnetic, we would have watched the monotonic decrease in S with increase in Bi^{3+} concentration. Furthermore, the magnetic parameters were estimated.

Keywords: Maxwell-Wagner interfacial type of polarization, Cole-Cole plots, soft magnetic material, solution combustion method

1. Introduction

Nowadays, manganese (Mn) ferrite nanoparticles have been used for great potential applications such as absorbing electromagnetic waves, storage media,

and water treatment catalysts [1–4]. Many researchers focused on the fabrication of spinel ferrite nanoparticles due to their exceptional electrical and magnetic properties [5–9]. To a progressively essential degree, the expanded scaling down and data storage devices of new devices require the utilization of nanosized magnetic attractive particles [10, 11]. Manganese spinel ferrite nanoparticles have gotten expanding consideration for their surprising magnetic properties, such as moderate saturation magnetization (M_s) and low coercivity with a mechanical hardness, high permeability, and good chemical stability [12, 13]. The significance of thick manganese (Mn) spinel ferrites additionally lies in their potential application, for example, transformers, core materials for coils, information and communication devices, and so forth. The $MnFe_2O_4$ nanoparticles have a spinel cubic structure having the general formula AB_2O_4, where the A sites are occupied by the Mn^{2+} ions and B sites by the Fe^{3+} ions. In a unit cell of manganese ferrites, there are 8 divalent Mn^{2+} ions, 16 trivalent Fe^{3+} ions, and 32 oxygen ions [14].

The spinel $MnFe_2O_4$ nanoparticles were prepared by synthesis methods such as sonochemical technique, co-precipitation, sol-gel method, and solution combustion method [15–17]. In the current work, the solution combustion method is often chosen because it is safe, cheap, and easy and it requires less time and energy for the preparation of nanoparticles. It also produces a high-purity product. In this method, the crystallite size, particle size, purity, surface area, degree of nature, and porosity can be influenced by the fuel (F) type [18]. However, for the preparation of nanoparticles, there is no requirement for complex tools, high-temperature furnaces, and reaction chambers in the synthesis process.

In the present work, the Bi^{3+}-substituted $MnFe_2O_4$ spinel nanoparticles were prepared by a solution combustion method using a mixture of fuels such as glucose and urea. The structural, microstructural, dielectrical, and magnetic properties of Bi-doped manganese spinel ferrite nanoparticles were synthesized and investigated through XRD, SEM, EDS, and dielectric and vibrating sample magnetometer (VSM) for photonic applications.

2. Experimental details

2.1 Materials

For the preparation of $Mn_{1-x}Bi_xFe_2O_4$ (x = 0.0, 0.05, 0.1, 0.15, and 0.2) nanoparticles, $Mn(NO_3)_2.4H_2O$ (manganese nitrate) (Sigma-Aldrich; molecular weight 251.01 g/mol, purity 99.0%), $Bi(NO_3)_3{\cdot}5H_2O$ (bismuth nitrate) (Leica, Sigma-Aldrich; purity 98 + %, molecular weight 485.07 g/mol), and $Fe(NO_3)_2.9H_2O$ (ferric nitrate) (Merck; purity 99.0%, molecular weight 404 g/mol) are used as oxidizers (O) and NH_2CONH_2 (carbamide) (Fisher Scientific; purity 99.0%, molecular weight 60.06 g/mol) and $C_6H_{12}O_6$ (glucose) (Glucomin-D; purity 99.4%, molecular weight 180.156 g/mol) as fuels. Further based on the oxidizer's and fuel's valences of the compounds, the oxidizer-and-fuel ratio is maintained to unity.

2.2 Synthesis method

The $Mn_{1-x}Bi_xFe_2O_4$ (x = 0.0, 0.05, 0.1, 0.15, and 0.2) spinel nanoparticles were prepared by the solution combustion method using a stoichiometric amount of O and a mixture of F proportions taken as one. Stoichiometric

amounts of manganese nitrate ($Mn(NO_3)_2{\cdot}4H_2O$), bismuth nitrate ($Bi(NO_3)_3{\cdot}5H_2O$), ferric nitrate ($Fe(NO_3)_3{\cdot}9H_2O$), carbamide (NH_2CONH_2), and glucose ($C_6H_{12}O_6$) are carried and put in a 500-ml Borosil glass beaker, which is then diluted with a double distilled water. The mixture solution was kept on magnetic stirrer about 60 min to get a homogeneous solution. This homogeneous solution was kept in a pre-warmed suppress heater at 450°C. Within 20 min, the burning process was finished. Then, the obtained powder was grained about 30 min using agate mortar and pestle. The flow chart of the $Mn_{1-x}Bi_xFe_2O_4$ (where x = 0.0, 0.05, 0.1, 0.15, and 0.2) solution combustion is shown in **Figure 1**.

2.3 Characterizations

The XRD patterns were gotten by using CuK_α radiation having a wavelength (λ) = 1.5406 Å, and the 2θ values run from 10° to 80° under the step size of 0.02°. The crystalline nature and phase structure can be understood from the XRD patterns. The SEM and EDS micrographs were collected by using JEOL (model JSM-840) to obtain the surface morphology and elemental composition of the samples. To study the electrical properties, the samples are made into pellets using a hydraulic press under the 5-ton pressure using an 11-mm die set. The prepared pellets are sintered at 650°C for 3 h. The sintered pellets are silver coated for a good electrical contact. The electrical properties of all samples are tested at room temperature in the frequency up to 20 MHz using the Wayne Kerr 6500B Series Impedance Analyzer. The magnetic properties were measured at room temperature using a physical properties measurement system (PPMS; Quantum Design, Inc.) up to a field of 20 kOe.

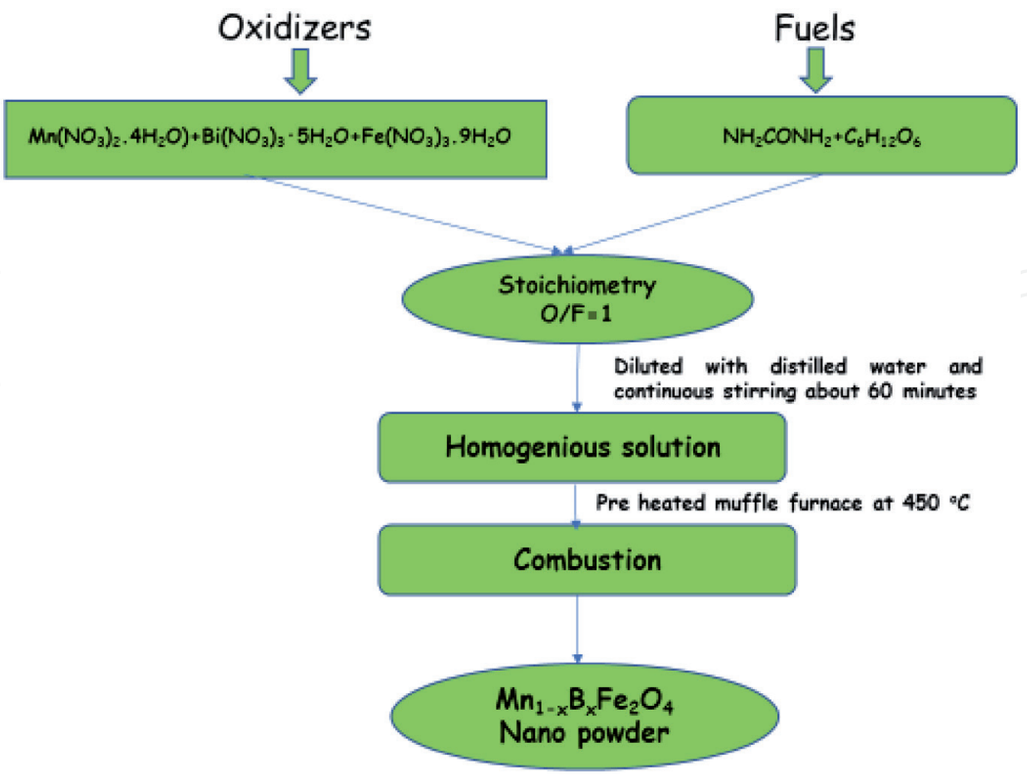

Figure 1.
The flow chart of the solution combustion method for $Mn_{1-x}Bi_xFe_2O_4$ (where x = 0.0, 0.05, 0.1, 0.15, and 0.2) nanoparticles.

3. Results and discussions

3.1 Phase, crystallinity, and structural elucidation

Figure 2 depicts the refined XRD patterns of $Mn_{1-x}Bi_xFe_2O_4$ (where x = 0.0, 0.05, 0.1, 0.15, and 0.2) as synthesized ferrite samples were plotted using a WinPLOTR program. The Bragg diffraction peaks corresponding to angular positions were indexed as (220) (311) (222) (400) (331) (422) (511) (440). Rietveld refinement was employed using a FullProf program for structural refinements. The parameters obtained from refinement, such as weighted (R_p) and unweighted (R_{wp})

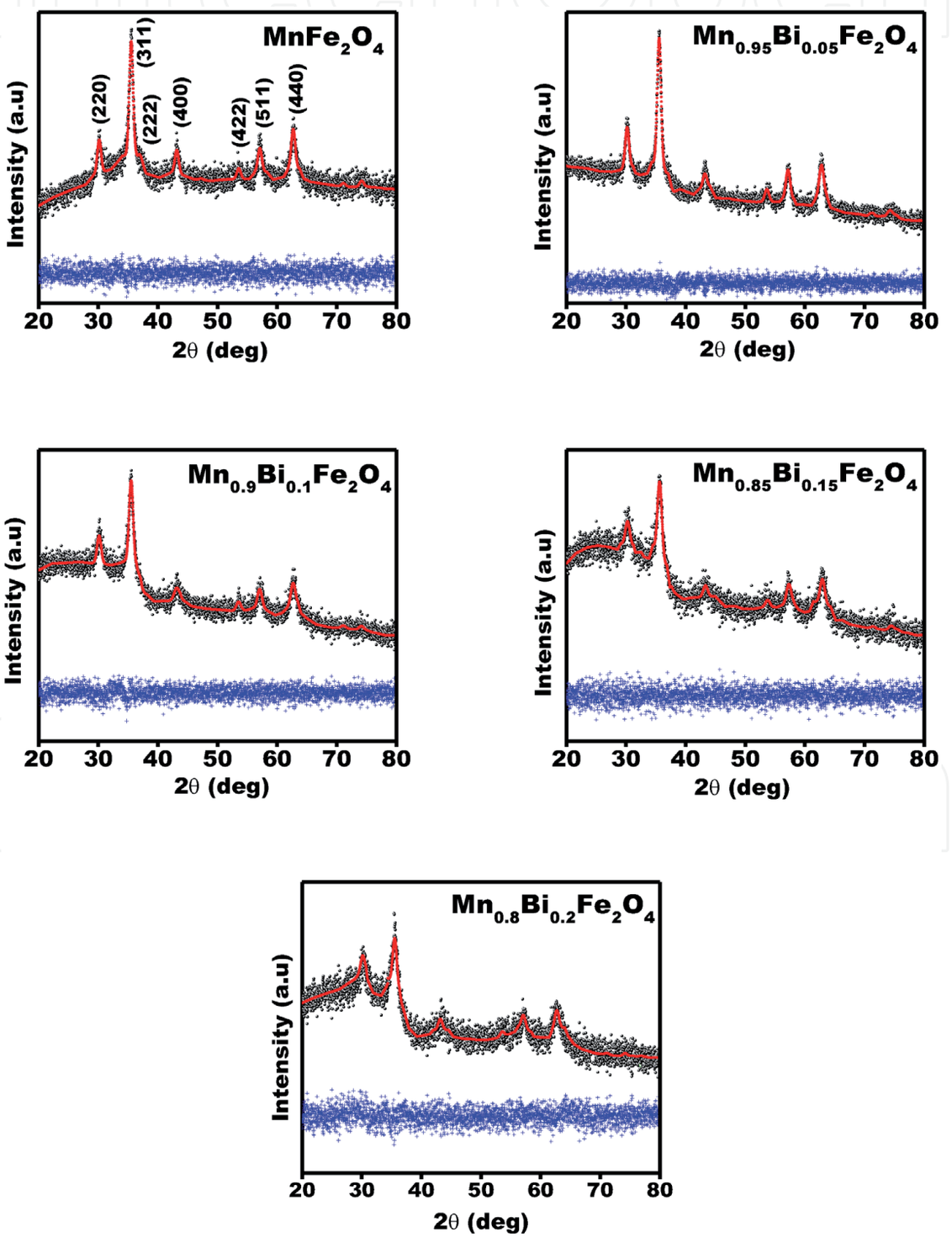

Figure 2.
Rietveld-refined XRD patterns of $Mn_{1-x}Bi_xFe_2O_4$ (where x = 0.0, 0.05, 0.1, 0.15, and 0.2) nanoparticles.

profile factor ratio (R_{wp}/R_p), which is less than one, and goodness-of-fit factor (χ^2), which is low, are given in **Table 1**. The refined XRD patterns confirm the single phase with a spinel cubic structure having a space further without any additional impurity peaks. The indexed (hkl) values are well matched with the Joint Committee of Powder Diffraction Standards (JCPDS) card number 74-2400. **Figure 3** clearly shows that the lattice parameters increase with the increase of Bi^{3+} concentration due to the difference in ionic radius of Mn^{2+} and Bi^{3+} ions. The ionic radius of Mn^{2+} (0.83 Å) is less than the ionic radius of Bi^{3+} (1.03 Å). The average crystallite size was calculated by using the equation below [19]:

$$D = \frac{k\lambda}{\beta cos\theta} \text{ nm} \quad (1)$$

where k is the Scherrer constant (k = 0.9), λ is the wavelength of Cu-k_α radiation, β is the full width half maximum, and θ is the angle of diffraction. The estimated crystallite size decreases with the increase of Bi^{3+} concentration (**Figure 3**). Further internal strain, X-ray density, and hopping length were increased with Bi^{3+} concentration increasing (**Figure 4**). The lattice parameters, average crystallite size, internal strain, X-ray density, and hopping lengths were tabulated in **Table 1**.

Bi^{3+} content	Lattice parameters (Å)	Crystallite size D in (nm)	Volume ($Å^3$)	Internal strain Є 10^{-2} (%)	X-ray density (Δ) g/cm^3	Hoping length (Å)	
						L_A	L_B
0.0	8.3612	13.7	584.52	88	5.2406	3.6025	2.9561
0.05	8.3658	11.9	585.49	95	5.4068	3.6225	2.9577
0.10	8.3845	10.8	589.42	96	5.5443	3.6306	2.9643
0.15	8.3874	10.6	590.04	105	5.7117	3.6319	2.9654
0.20	8.3932	9.2	591.26	131	5.8731	3.6343	2.9674

Table 1.
Crystallite size, lattice constant, strain, X-ray density, magnetic hoping length data of $Mn_{1-x}Bi_xFe_2O_4$ (where x = 0.0, 0.05, 0.1, 0.15, and 0.2) nanoparticles.

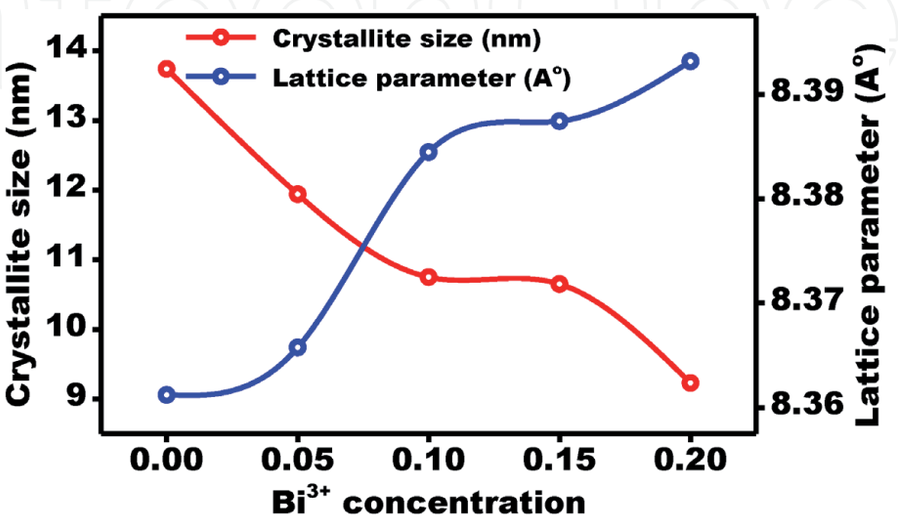

Figure 3.
Variation of crystallite size (nm) and lattice parameter (a°) with Bi^{3+} doping concentration of $Mn_{1-x}Bi_xFe_2O_4$ (where x = 0.0, 0.05, 0.1, 0.15, and 0.2) nanoparticles.

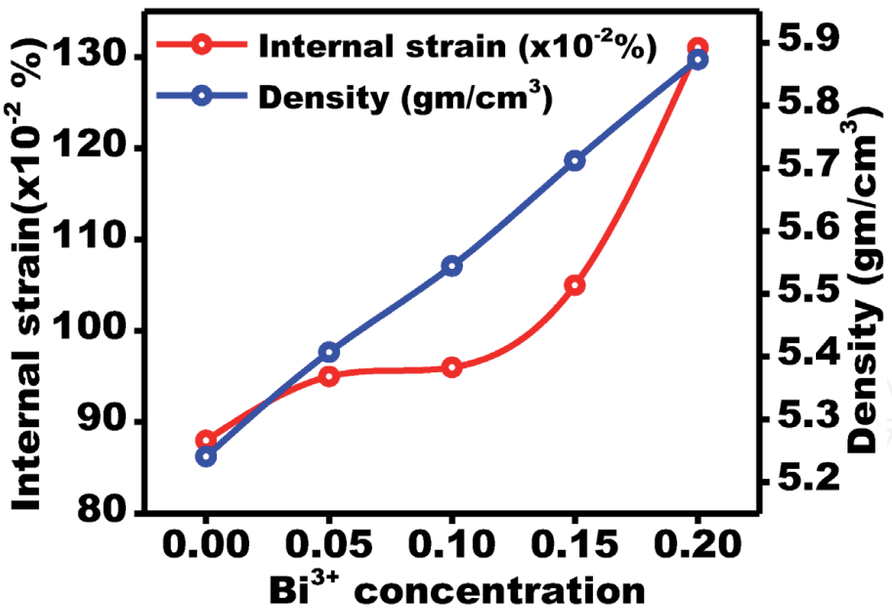

Figure 4.
Variation of internal strain (%) and density (gm/cm³) of (where x = 0.0, 0.05, 0.1, 0.15, and 0.2) nanoparticles with Bi^{3+} doping concentration.

3.2 SEM and EDS

Figures 5 and **6** show the SEM and EDS of Bi^{3+}-doped $MnFe_2O_4$ (where x = 0.0, 0.05, 0.1, 0.15, and 0.2) ferrite samples synthesized, respectively. All SEM micrographs reveal the highly porous nature of the samples [20]. All the samples show the dry foamy powder due to the combustion. The average grain size cannot be observed due to the high porous nature of the sample. The density of samples increases with Bi^{3+} concentration. The EDS images clearly reveal that Mn, Fe, and O peaks are clearly visible in all samples. The Bi^{3+} peak is visible in all samples except at 0 mol % Bi^{3+} sample. The stoichiometry of constituent elements present in the $Mn_{1-x}Bi_xFe_2O_4$ with x = 0.0, 0.05, 0.1, 0.15, and 0.2 ferrite nanoparticles estimated from EDS spectrum is shown in **Table 2**. The estimated stoichiometry as listed in **Table 3** is very near to the composition of theoretical values.

3.3 Dielectric studies

3.3.1 Real (ε′) and imaginary (ε″) parts of dielectric constant

The real (ε′) and imaginary (ε′′) parts of the dielectric constant as a function of frequency at room temperature for $Mn_{1-x}Bi_xFe_2O_4$ (where x = 0.0, 0.05, 0.1, 0.15, and 0.2) nanoparticles are depicted in **Figure 7(a)** and **Figure 7(b)**, respectively. At low frequency, the real and imaginary parts of dielectric constants show the dispersion for all samples. The dielectric constant values sharply decrease with increasing in frequency, and it is due to Maxwell-Wagner interfacial-type polarization according to Koop's phenomenological theory [21]. At the lower-frequency region, the interfacial polarization contributes to the dispersion. A systematic variation is observed due to the dispersion of dielectric constant with substitution. At the higher-frequency region, it cannot follow the alternating electric field, so real and imaginary parts of dielectric constants are independent of frequency at that region. In ferrites, the maximum dielectric constant is observed in samples having higher Fe^{2+} content. At the lower-frequency region, the hopping (exchange

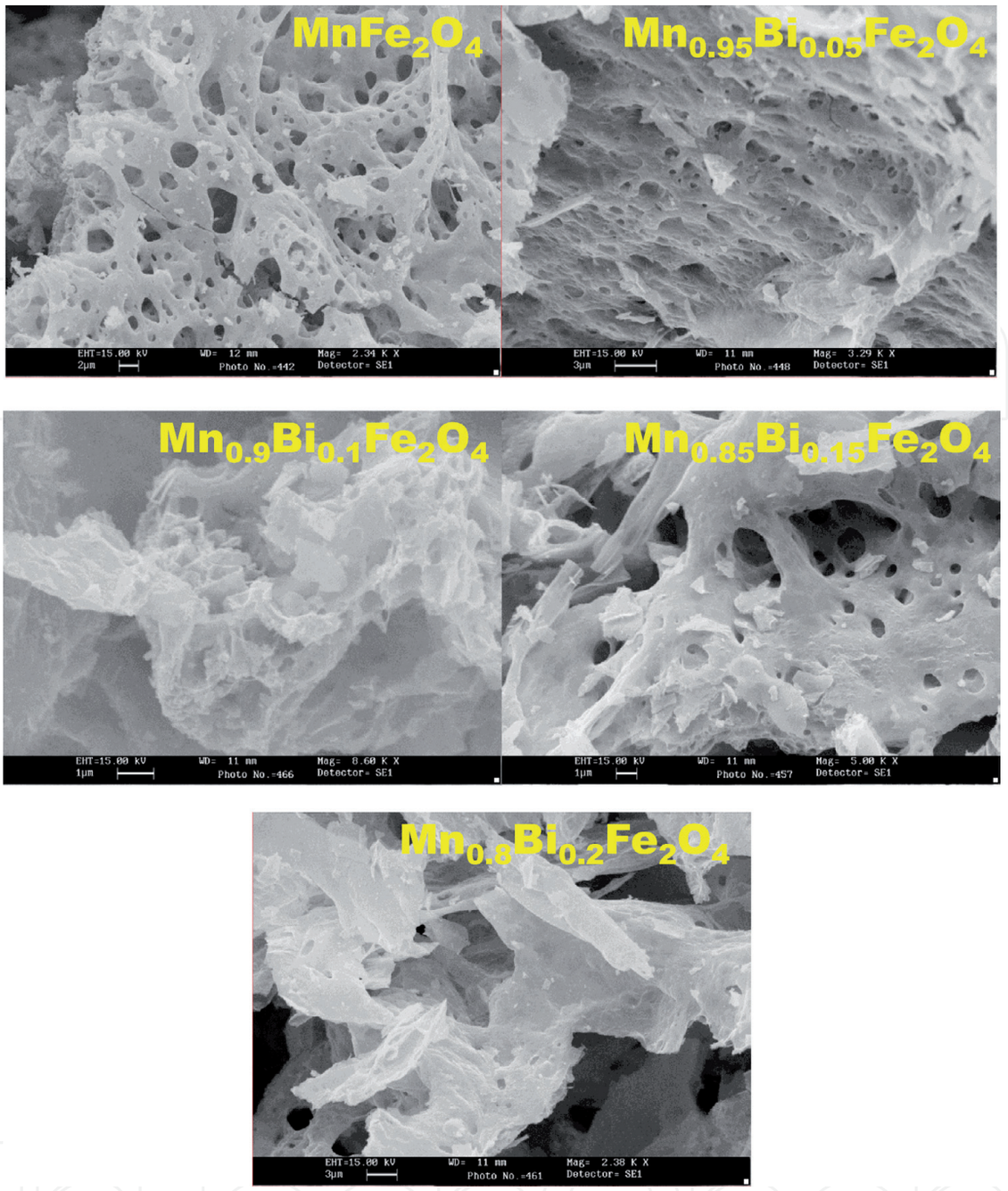

Figure 5.
SEM micrograph images of $Mn_{1-x}Bi_xFe_2O_4$ ferrite nanoparticles with x = 0.0 ($MnFe_2O_4$), x = 0.05 ($Mn_{0.95}Bi_{0.05}Fe_2O_4$), x = 0.1 ($Mn_{0.9}Bi_{0.1}Fe_2O_4$), x = 0.15 ($Mn_{0.85}Bi_{0.15}Fe_2O_4$), and x = 0.2 ($Mn_{0.8}Bi_{0.2}Fe_2O_4$).

of electron) between Fe^{2+} and Fe^{3+} at octahedral sites follows the alternating electric field. Many literatures on AB_2O_4 ferrites indicate that high-temperature sintering leads to the exchange of the Fe^{3+} ions to Fe^{2+} ions at octahedral sites to some degree [22]. However, the hopping process, involving between the Fe^{3+} and Fe^{2+} ions, is attributed to the dielectric properties of the samples. Thus, the increase of Bi^{3+} concentration results in the increase of dielectric constant. The grain size also influences the dielectric properties, since, in ferrite samples, the dielectric constant of the poorly conducting grain boundary is less than the dielectric constant of highly conducting grains. Thus, size reduction introduces more grain boundaries and hence increases changes in electron polarization at the grain boundaries. Since the size decreases with bismuth substitution increasing, it also increases the dielectric constant.

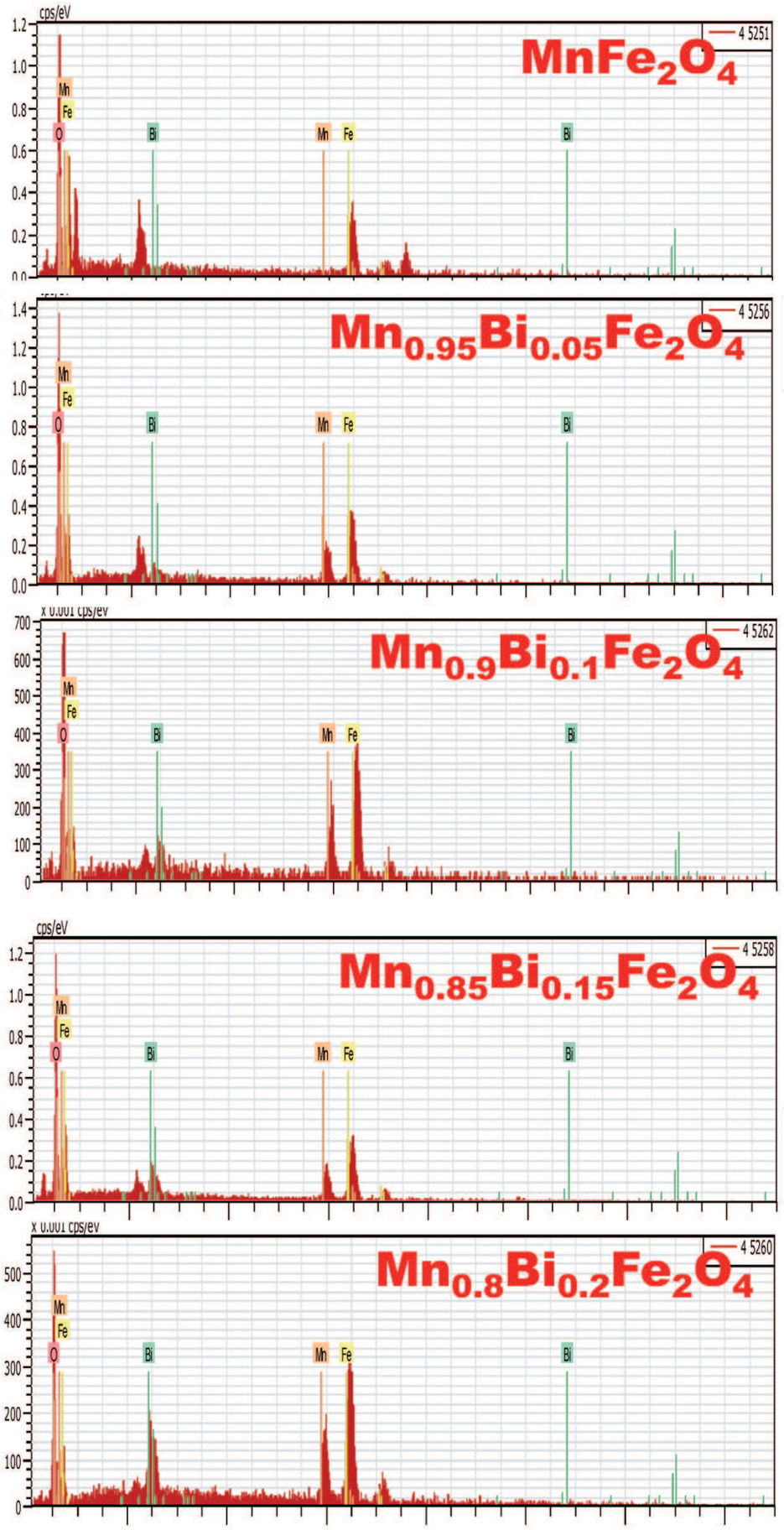

Figure 6.
EDS patterns of $Mn_{1-x}Bi_xFe_2O_4$ ferrite nanoparticles with x = 0.0 ($MnFe_2O_4$), x = 0.05 ($Mn_{0.95}Bi_{0.05}Fe_2O_4$), x = 0.1 ($Mn_{0.9}Bi_{0.1}Fe_2O_4$), 0.15 ($Mn_{0.85}Bi_{0.15}Fe_2O_4$), and x = 0.2 ($Mn_{0.8}Bi_{0.2}Fe_2O_4$).

x	Atomic abundance of elements (%)				
	Mn	**Bi**	**Fe**	**O**	**Total**
0.0	17.92	0.0	32.13	49.96	100
0.05	20.45	0.96	29.07	49.52	100
0.1	18.59	1.75	30.53	49.12	100
0.15	19.37	3.11	29.08	48.44	100
0.2	20.02	4.30	27.83	47.85	100

Table 2.
The stoichiometry of constituent elements present in the $Mn_{1-x}Bi_xFe_2O_4$ (where x = 0.0, 0.05, 0.1, 0.15, and 0.2) nanoparticles estimated from EDS spectrum.

Bi^{3+} concentration (x)	Element	Composition of theoretical values	Composition from EDX analysis
	Mn	1	0.99
0	Bi	0	0
	Fe	1	1
	Mn	0.95	0.955
0.05	Bi	0.05	0.045
	Fe	1	1
	Mn	0.9	0.914
0.1	Bi	0.1	0.086
	Fe	1	1
	Mn	0.85	0.862
0.15	Bi	0.15	0.138
	Fe	1	1
	Mn	0.8	0.823
0.2	Bi	0.2	0.177
	Fe	1	1

Table 3.
Summary of EDS analysis of $Mn_{1-x}Bi_xFe_2O_4$ (where x = 0.0, 0.05, 0.1, 0.15, and 0.2) nanoparticles.

3.3.2 Dielectric loss tangent (tan δ)

The dielectric loss tangent as a function of frequency at room temperature for $Mn_{1-x}Bi_xFe_2O_4$ (where x = 0.0, 0.05, 0.1, 0.15, and 0.2) nanoparticles is shown in **Figure 8**. The figure shows the dielectric loss tangent decreases with the increase of the frequency. The dielectric loss tangent is a result of the string in polarization in accordance with the applied external electric field. The materials with high dielectric loss tangent are engaged for manufacturing high-frequency heating devices. The tan δ was calculated using the relation $\tan\delta = \varepsilon'/\varepsilon''$, where ε' and ε'' are the real and imaginary parts of the dielectric constant, respectively [23].

The tan δ decreases with the increase of the frequency, and then it becomes constant at higher frequencies for all samples. The dielectric loss tangent depends on a number of factors, such as homogeneity, stoichiometry, synthesis method,

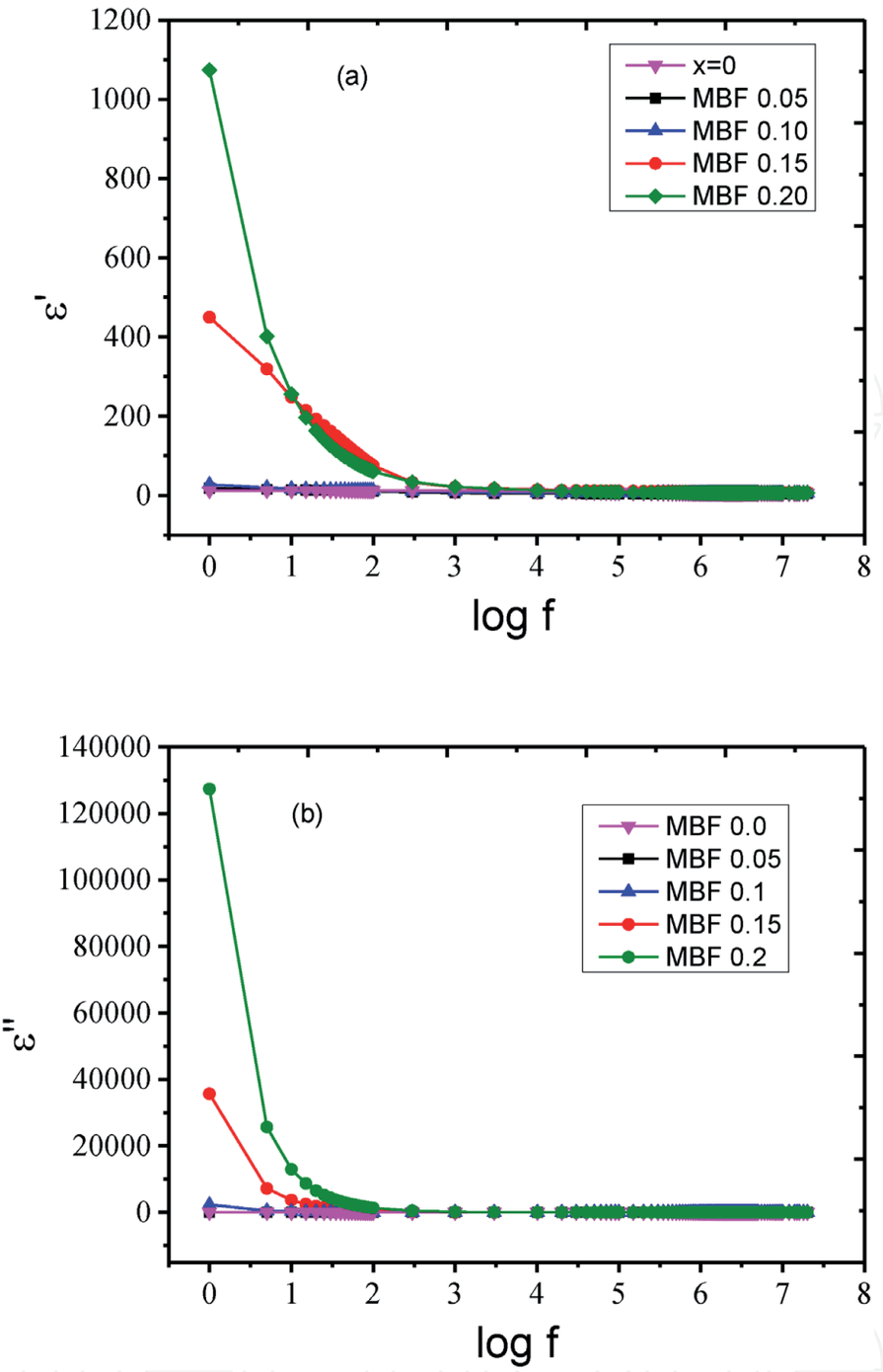

Figure 7.
(a) The real (ε′) and (b) imaginary (ε″) parts of the dielectric constant as a function of frequency at room temperature, respectively, for $Mn_{1-x}Bi_xFe_2O_4$ (where x = 0.0, 0.05, 0.1, 0.15, and 0.2) nanoparticles.

ferric content, and composition. The frequency increases with the decrease of the dielectric loss tangent; it may be characterized by the Maxwell-Wagner polarization and conduction mechanism in ferrites.

3.3.3 AC conductivity (σ_{ac})

The variation of σ_{ac} as a function of frequency at room temperature for $Mn_{1-x}Bi_xFe_2O_4$ (where x = 0.0, 0.05, 0.1, 0.15, and 0.2) nanoparticles is shown in **Figure 9**. From the figure, it may well be seen that at first the conductivity stays steady in the low frequencies, bit by bit increments in the middle of the road frequencies, and afterward shows scattering for high frequencies in consistence with the Jonscher power law. The AC conductivity was calculated by using the equation

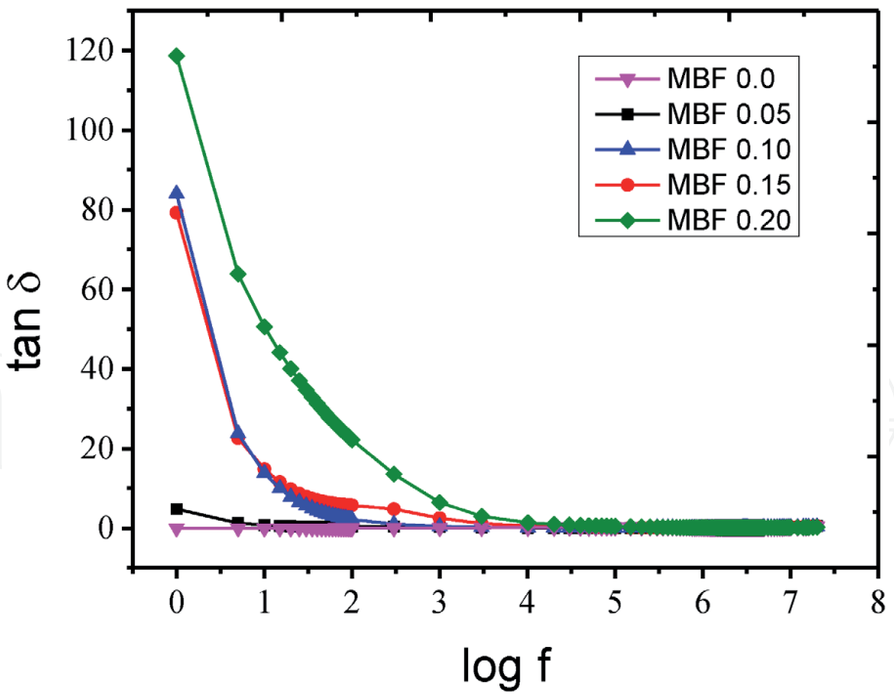

Figure 8.
The dielectric loss tangent as a function of frequency at room temperature for $Mn_{1-x}Bi_xFe_2O_4$ (where x = 0.0, 0.05, 0.1, 0.15, and 0.2) nanoparticles.

$\sigma_{ac} = 2\pi f \varepsilon_0 \times \tan\delta$, where ε_0 is the permittivity of free space, f is the frequency, and tan δ is the dielectric loss tangent. Here, the figure shows that σ_{ac} increases with the increase of the frequency according to the hopping model [24]. In the lower frequencies, grain limits are increasingly adequate; thus the recurrence-free conducts are accomplished. Be that as it may, at high-frequency system, the increase in σ_{ac} is credited to the increased hopping of charge bearers between the Fe^{2+} and Fe^{3+} particles and Mn^{2+} and Mn^{3+} particles at the octahedral site and further as a

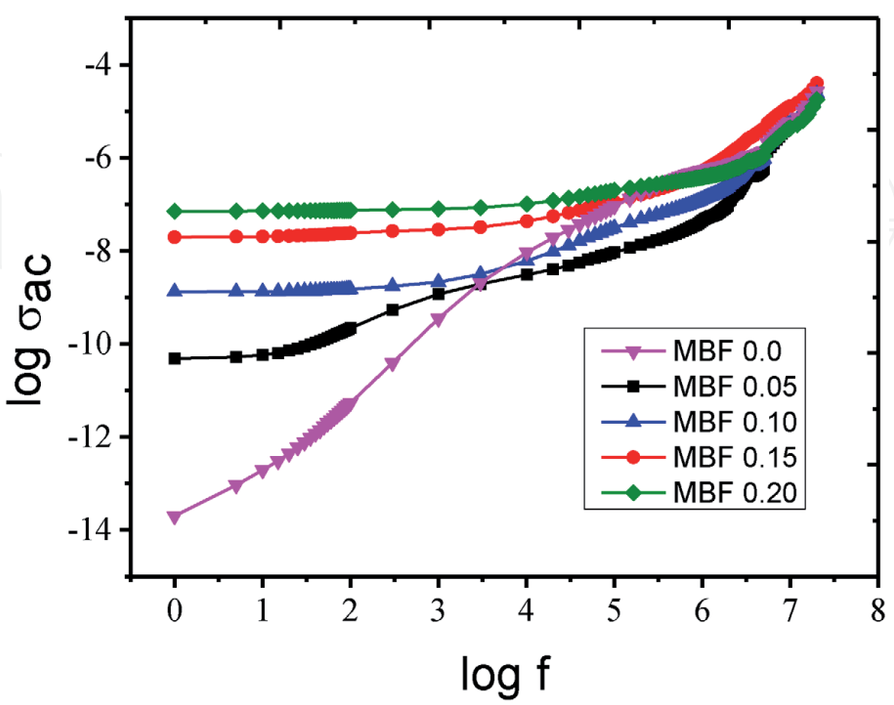

Figure 9.
The AC conductivity as a function of frequency at room temperature for $Mn_{1-x}Bi_xFe_2O_4$ (where x = 0.0, 0.05, 0.1, 0.15, and 0.2) nanoparticles.

result of grain impact. With increasing substitution of Bi^{3+} by Mn^{2+} particles, it very well may be seen that at first conductivity diminishes because of the decrease in the quantity of Mn^{2+}-Mn^{3+} particles which confines the portability of charge transporters at the octahedral destinations.

3.3.4 Real and imaginary parts of complex impedance

Figure 10(a) and **(b)** shows the real and imaginary parts of complex impedance as a function of frequency at room temperature for $Mn_{1-x}Bi_xFe_2O_4$ (where x = 0.0, 0.05, 0.1, 0.15, and 0.2) nanoparticles, respectively. These types of frequency dependence complex impedance have been used for the study of the contribution of grains and grain boundaries on the electrical properties of nanoferrites. The obtained results showed the complex impedance versus frequency for the cobalt

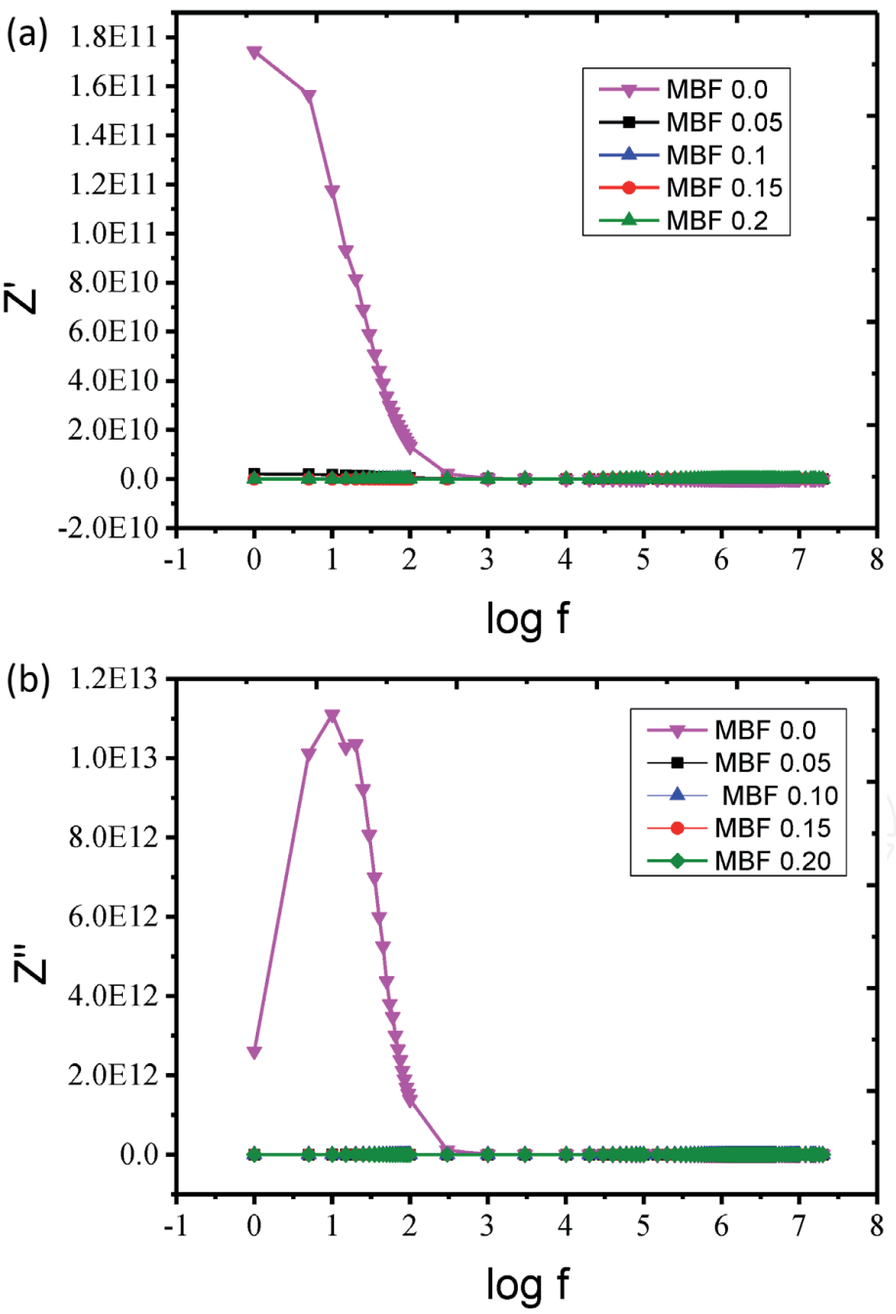

Figure 10.
(a) and (b) The real and imaginary parts of complex impedance as a function of frequency at room temperature for $Mn_{1-x}Bi_xFe_2O_4$ (where x = 0.0, 0.05, 0.1, 0.15, and 0.2) nanoparticles.

ferrites. **Figure 10(a)** indicates that the magnitude of the real part of dielectric constant Z′ decreased with the increase of frequency. The real part of dielectric constant curves tended to merge in the high-frequency region. Such behavior is related to the effect of space charge polarization in the material [25]. **Figure 10(b)** indicates that the imaginary part of dielectric constant Z′′ reached a maximum value at the low-frequency region and then decreased with further increasing of the frequency, approaching a small value at high-frequency region. Further, it was observed that the height of the peak curve decreased with the concentration increasing, indicating a decrease in the relaxation time. The observed relaxation peak in the magnitude of Z′′ demonstrated the existence of space charge relaxation.

3.3.5 Cole-Cole plot

Figure 11 shows the Cole-Cole plots of $Mn_{1-x}Bi_xFe_2O_4$ (where x = 0.0, 0.05, 0.1, 0.15, and 0.2) nanoparticles at room temperature. Cole-Cole plot shows the real part complex impedance (Z′) and the imaginary part of complex impedance (Z′′) along x-axis and y-axis, respectively. **Figure 11** clearly shows one semicircle was obtained for each of the samples, due to the grain boundary effect. The effects of grain boundary of the material are contributed by the parallel combination of grain boundary resistance and capacitance. However, the radius of curvature of each semicircular arc is reasonably shifted from the magnitude of Z′ when the concentration increased, which is attributed to the presence of a non-Debye type of relaxation phenomenon [26]. Further, the radius of curvature of each semicircular arc is indirectly proportional to the electrical conductance of the material and directly proportional to the electrical resistance. The position of the semicircular arc depends on its relaxation times.

3.3.6 The real (M′) and imaginary (M″) parts of electric modulus

Figure 12(a) and **(b)** shows the real (M′) and imaginary (M′′) parts of electric modulus as a function of frequency at room temperature for $Mn_{1-x}Bi_xFe_2O_4$ (where

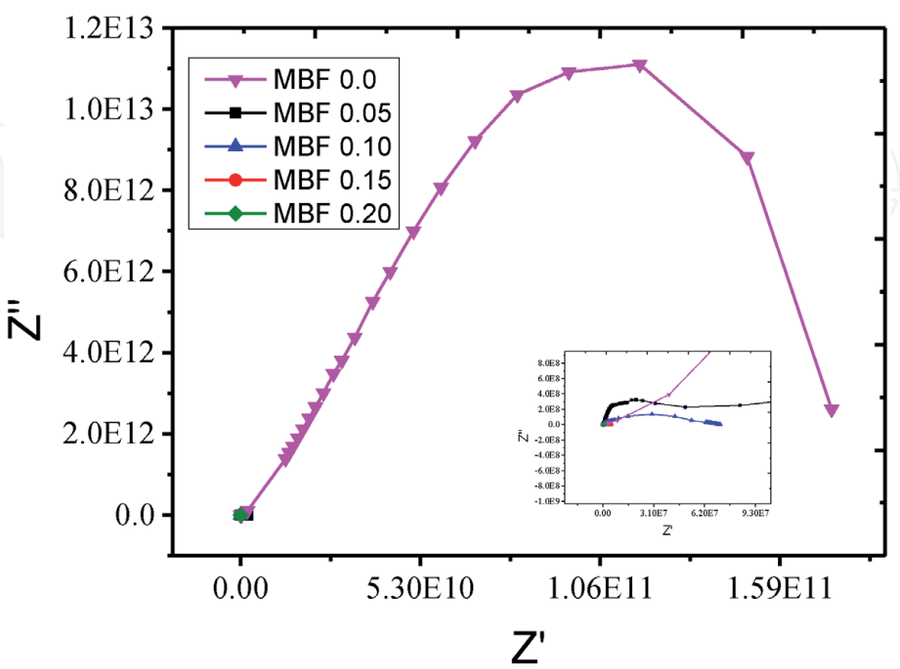

Figure 11.
The Cole-Cole plots of $Mn_{1-x}Bi_xFe_2O_4$ (where x = 0.0, 0.05, 0.1, 0.15, and 0.2) nanoparticles at room temperature.

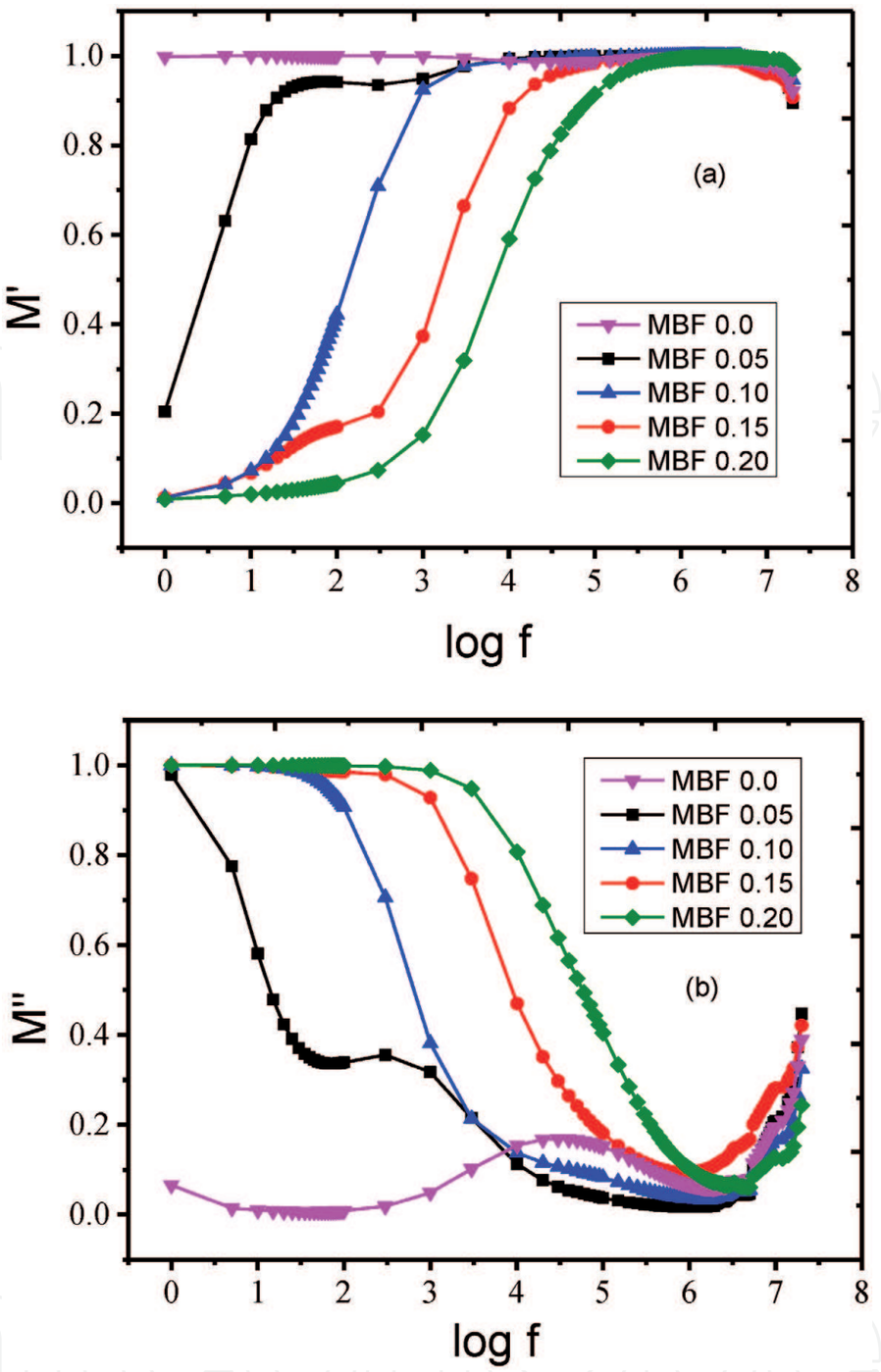

Figure 12.
(a) and (b) The real (M′) and imaginary (M″) parts of electric modulus as a function of frequency at room temperature for $Mn_{1-x}Bi_xFe_2O_4$ (where x = 0.0, 0.05, 0.1, 0.15, and 0.2) nanoparticles.

x = 0.0, 0.05, 0.1, 0.15, and 0.2) nanoparticles, respectively. M′ approaches zero in lower-frequency district and shows constant scattering moving in midfrequency area, while it displays a level sort conduct in higher frequency. This sort of conduct is emerged from the unimportant electrode polarization in lower frequencies and short-range and long-range versatility of charge transporters contributing for the conduction wonders in midfrequencies and recurrence-free electrical conduction in higher frequencies, individually [27]. Also, the focus increment M′′ shows the unwinding tops from lower-frequency area to higher-frequency area. The relaxation tops moving plainly demonstrate the spread of relaxation time of the material. The presence of relaxation tops at lower-, center-, and higher-frequency areas is ascribed to the commitment of capacitance to the grain limit, structural, and grain stage attributes, separately, which is very much concurred with the revealed writing.

3.3.7 Nyquist plot

Figure 13 gives out the variation of complex electric modulus spectrum (Nyquist plot) (M′ vs. M′′) at room temperature for $Mn_{1-x}Bi_xFe_2O_4$ (where x = 0.0, 0.05, 0.1, 0.15, and 0.2) nanoparticles, and it shows the single semicircular segment for all samples, which is beginning from the grain limit commitments of the material. The Nyquist plot reveals the presence of a non-Debye type of relaxation phenomenon, which is further validated from the electrical modulus analysis [28]. Also, each crescent bend is almost overlapped with each other and no variety is observed, which calls attention to the nearness of electrical unwinding process in the material.

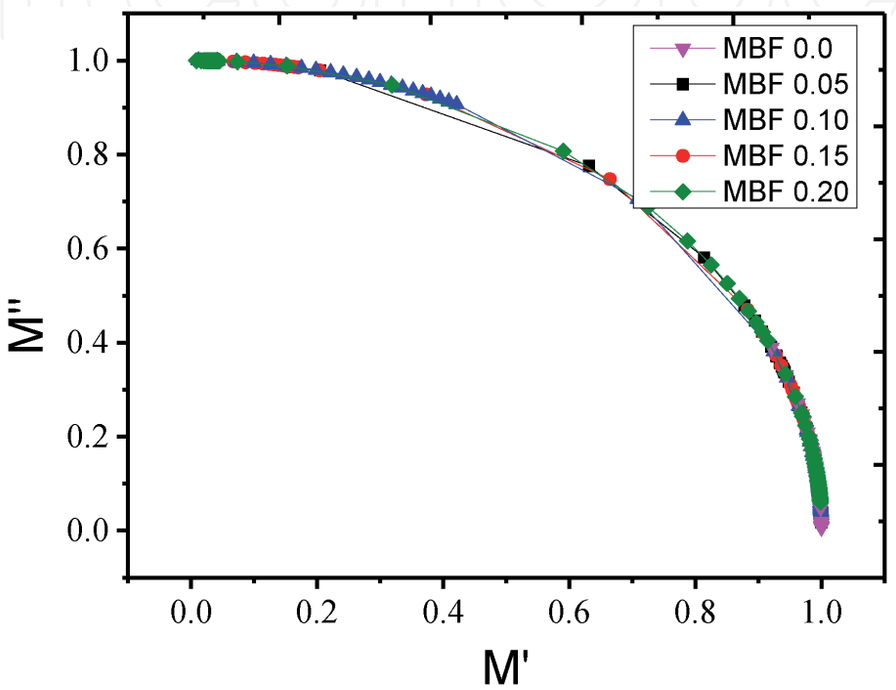

Figure 13.
Nyquist plot of $Mn_{1-x}Bi_xFe_2O_4$ (where x = 0.0, 0.05, 0.1, 0.15, and 0.2) nanoparticles at room temperature.

3.4 Magnetic properties

At room temperature, magnetic hysteresis (M-H) curves of $Mn_{1-x}Bi_xFe_2O_4$ (where x = 0.0, 0.05, 0.1, 0.15, and 0.2) nanoparticles show very narrow hysteresis loops, which confirms the soft magnetic material nature as depicted in **Figure 14**. The magnetization measurement was done by using VSM mounted with maximum applied field of 2 T at room temperature.

The remanent magnetization (M_r) and M_s was estimated by the M-H loop of the y-axis (magnetization axis). The coercivity field (H_c) was estimated by the M-H loop of the x-axis (field axis). The remanence ratio (S) was calculated by using equation $S = M_r/M_s$. The magneton number (η_B) was calculated by using equation $\eta_B = \frac{M.W\,X\,M_s}{5585}$. The cubic anisotropy ($K_c$) was calculated by using the equation $K_c = \frac{H_c X M_s}{0.64}$. The uniaxial anisotropy (K_u) was calculated by using the equation $K_u = \frac{H_c X M_s}{0.985}$ [8, 29]. At room temperature, the magnetic parameters such as M_r, M_s, H_c, S, η_B, K_c, and K_u decrease with the increase of Bi^{3+} concentration (**Figures 15–17**). In ferrites, the coercive force is gotten by inversion of the direction of the divider development and that of domain turning around the bearing of the applied field. Generally, the successful sticking for domain wall causes the coercivity; it is understood that the greater grain size reduces H_C [30]. In the present examination, the coercive values

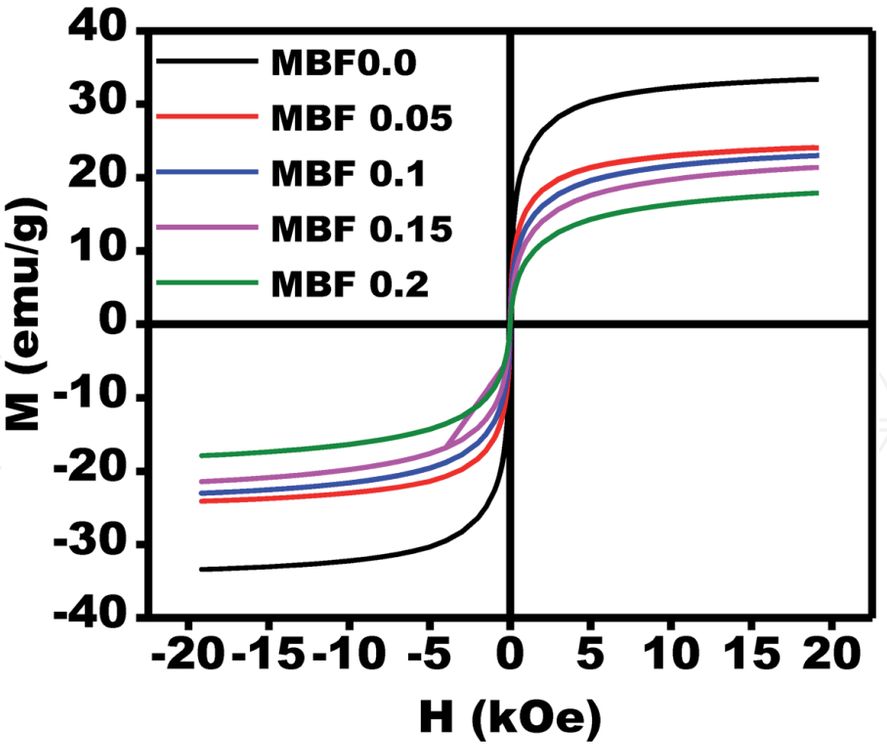

Figure 14.
M-H loops measured at room temperature for $Mn_{1-x}Bi_xFe_2O_4$ (MBF) ferrite nanoparticles with x = 0.0, 0.05, 0.1, 0.15, and 0.2 nanoparticles.

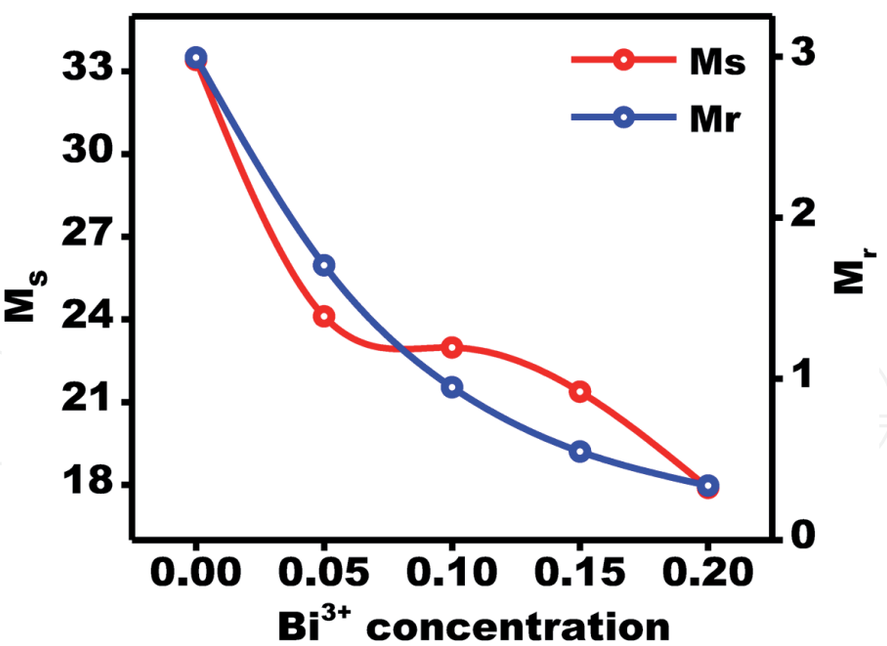

Figure 15.
Variation of M_S and M_r of $Mn_{1-x}Bi_xFe_2O_4$ with x = 0.0, 0.05, 0.1, 0.15, and 0.2 ferrite nanoparticles with Bi^{3+} doping concentration.

are low; thus, the likelihood of domain rotation is lower. The materials with bigger grain size have been used to accomplish lower core loss. Strikingly, as anticipated, the estimation of the reduced remanence value was found to be the lowest for x = 0.20 concentration sample (**Table 4**). We observed S esteems began interestingly from the higher super paramagnetic and the monotonic decrease in S with

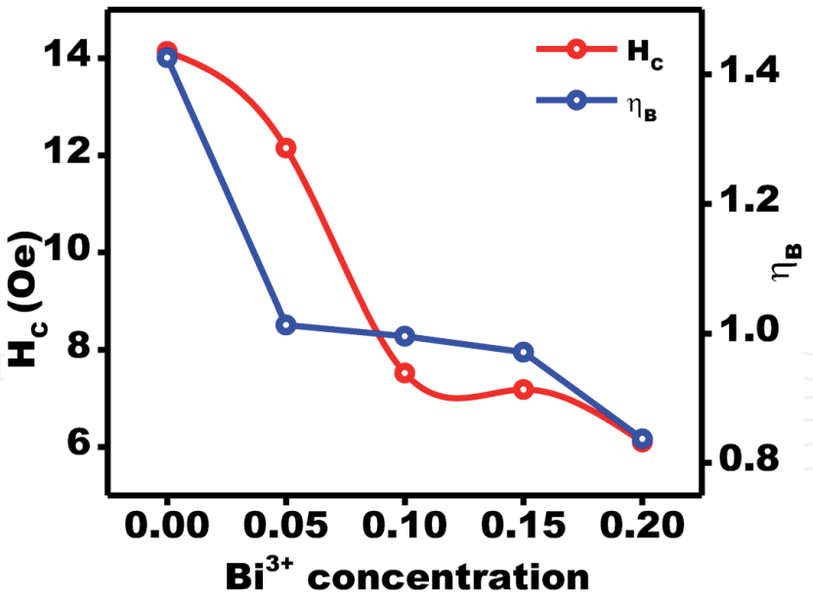

Figure 16.
Variation of H_C and η_B of $Mn_{1-x}Bi_xFe_2O_4$ with x = 0.0, 0.05, 0.1, 0.15, and 0.2 ferrite nanoparticles with Bi^{3+} doping concentration.

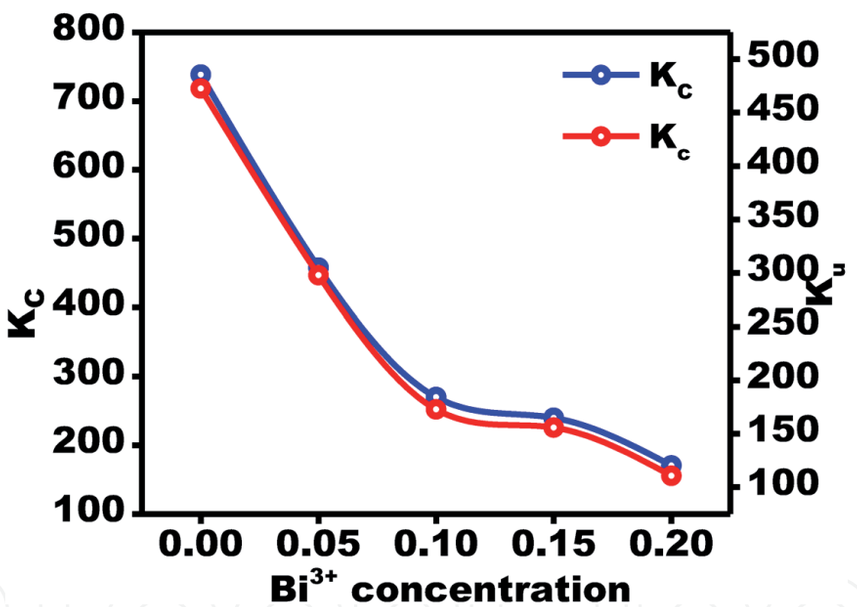

Figure 17.
Variation of K_C and K_u of $Mn_{1-x}Bi_xFe_2O_4$ with x = 0.0, 0.05, 0.1, 0.15, and 0.2 ferrite nanoparticles with Bi^{3+} doping concentration.

Bi^{3+} concentration (x)	M_S (emu/g)	M_r (emu/g)	H_c (Oe)	$S = M_r/M_S$	K_u (erg/cm^3)	K_c (erg/cm^3)	η_B (μ_B)
0.00	33.42	2.994	14.14	0.0896	472.55	738.37	1.4259
0.05	24.11	1.705	12.15	0.0707	297.93	457.71	1.0123
0.10	22.98	0.947	7.52	0.0412	172.80	270.02	0.9959
0.15	21.38	0.548	7.18	0.0256	155.84	239.86	0.9713
0.20	17.89	0.337	6.10	0.0189	110.79	170.49	0.8373

Table 4.
Room temperature magnetic parameters of $Mn_{1-x}Bi_xFe_2O_4$ (where x = 0.0, 0.05, 0.1, 0.15, and 0.2), i.e., M_S, M_r, reduced S, (H_c), K_u, cubic anisotropy constant (K_c), and η_B.

increase in Bi^{3+} concentration. Thus, it is expected that the observed impact is overwhelmed by the surface pinning and the change in intrinsic magnetic anisotropy of the particles because of Bi doping.

4. Conclusion

The $Mn_{1-x}Bi_xFe_2O_4$ (where x = 0.0, 0.05, 0.1, 0.15, and 0.2) nanoparticles are synthesized by the solution combustion method using a mixture of fuels as carbamide and glucose. The crystallite sizes were found in nanometer, and the crystallite size decreases with the increase of Bi^{3+} concentration. The lattice parameter increases with the increase of Bi^{3+} concentration due to the difference in ionic radius of Mn^{2+} and Bi^{3+} ions. The porous nature of the samples was confirmed by scanning electron microscopy. The elemental composition was analyzed by EDS composition. The dielectric parameters such as real part and imaginary parts of dielectric constant and dielectric loss tangent decrease with the increase of frequency, and this behavior could be explained by a Maxwell-Wagner interfacial-type polarization. All dielectric parameters increase with the increase of Bi^{3+} concentration. The AC conductivity increases with the increase of frequency according to the hopping model. The real part of complex impedance decreases with the increase of frequency. The observed relaxation peak in the magnitude of imaginary part of complex impedance Z'' demonstrated the existence of space charge relaxation. The Cole-Cole plot reveals one semicircle was obtained for each of the samples, due to the grain boundary effect. It is attributed to the presence of a non-Debye type of relaxation phenomenon. The real and imaginary parts of electric modulus vary with frequency. The Nyquist plot reveals the presence of a non-Debye type of relaxation phenomenon, which is further validated from the electrical modulus analysis. The magnetic hysteresis curves of all samples reveal the soft magnetic material nature. The magnetic parameters such as remanent magnetization, saturation magnetization, and coercivity field were decreased with the increase of Bi^{3+} concentration. $Mn_{1-x}Bi_xFe_2O_4$ (where x = 0.0, 0.05, 0.1, 0.15, and 0.2) nanoparticles have great potential for photonic applications.

Author details

V. Jagadeesha Angadi[1*], H.R. Lakshmiprasanna[2] and K. Manjunatha[2]

1 Department of Physics, P.C. Jabin Science College, Hubballi, India

2 Department of Physics, School of Engineering, Presidency University, Bengaluru, India

*Address all correspondence to: jagadeeshbub@gmail.com

References

[1] Amighian J, Mozaffari M, Nasr B. Preparation of nano-sized manganese ferrite ($MnFe_2O_4$) via coprecipitation method. Physica Status Solidi. 2006;**3**:3188-3192

[2] Chen G, Wang J, Zhou L, Ma W, Zhang D, Ren F, et al. A facile solvothermal synthesis and magnetic properties of $MnFe_2O_4$ spheres with tunable sizes. Journal of the American Ceramic Society. 2012;**95**:3569-3576

[3] Hu W, Qin N, Wu G, Lin Y, Li S, Bao D. Opportunity of spinel ferrite materials in nonvolatile memory device applications based on their resistive switching performances. Journal of American Ceramic Society. 2012;**134**:14658

[4] Ji R, Cao C, Chen Z, Zhai H, Bai J. Solvothermal synthesis of $Co_xFe_{3-x}O_4$ spheres and their microwave absorption properties. Journal of Materials Chemistry C. 2014;**2**:5944

[5] Lee N, Hyeon T. Chemical Society Reviews. 2012;**41**:2575

[6] Arteaga-Cardona F, Pal U, Alonso JM, de la Presa P, Mendoza-Álvarez M-E, Salazar-Kuri U, et al. Tuning magnetic and structural properties of $MnFe_2O_4$ nanostructures by systematic introduction of transition metal ions M^{2+} (M=Zn, Fe, Ni, Co). Journal of Magnetism and Magnetic Materials. 2019;**490**:165496

[7] Li B, Cao H, Shao J, Qub M, Warner JH. Superparamagnetic Fe_3O_4 nanocrystals@graphene composites for energy storage devices. Journal of Materials Chemistry. 2011;**21**:5069

[8] Jagadeesha Angadi V, Anupama AV, Kumar R, Matteppanavar S, Rudraswamy B, Sahoo B. Observation of enhanced magnetic pinning in Sm^{3+} substituted nanocrystalline MnZn ferrites prepared by propellant chemistry route. Journal of Alloys and Compounds. 2016;**682**:263-274

[9] Zhang CF, Zhong XC, Yu HY, Liu ZW, Zeng DC. Effects of cobalt doping on the microstructure and magnetic properties of Mn-Zn ferrites prepared by the co-precipitation method. Physica B. Physics of Condensed Matter. 2009;**404**:2327-2331

[10] Lakshmiprasanna HR, Jagadeesha Angadi V, Babu BR, Pasha M, Manjunatha K, Matteppanavar S. Effect of Pr^{3+}-doping on the structural, elastic and magnetic properties of Mn-Zn ferrite nanoparticles prepared by solution combustion synthesis method. Chemical Data Collections. 2019;**24**:100273

[11] Srinivasamurthy KM, Manjunatha K, Sitalo EI, Kubrin SP, Sathish IC, Matteppanavar S, et al. Effect of Ce^{3+} substitution on the structural, morphological, dielectric, and impedance spectroscopic studies of Co–Ni ferrites for automotive applications. Indian Journal of Physics. 2019;**65**:1-12

[12] Arabi H, Moghadam NK. Nanostructure and magnetic properties of magnesium ferrite thin films deposited on glass substrate by spray pyrolysis. Journal of Magnetism and Magnetic Materials. 2013;**335**:144-148

[13] Godbole RV, Rao P, Alegaonkar PS, Bhagwat S. Influence of fuel to oxidizer ratio on LPG sensing performance of $MgFe_2O_4$ nanoparticles. Materials Chemistry and Physics. 2015;**161**:135-141

[14] Manjunatha K, Sathish IC, Kubrin SP, Kozakov AT, Lastovina TA, Nikolskii AV, et al. X-ray photoelectron spectroscopy and low temperature Mössbauer study of Ce^{3+} substituted $MnFe_2O_4$. Journal of Materials Science: Materials in Electronics. 2019;**30**:10162-10171

[15] Dutta DP, Manjanna J, Tyagi AK. Magnetic properties of sonochemically synthesized $CoCr_2O_4$ nanoparticles. Journal of Applied Physics. 2009;**106**:043915

[16] Durgesh K, Nemkovski K, Su Y, Rath C. Enhancement of Curie- and spin-spiral temperatures with doping Fe in multiferroic $CoCr_2O_4$ nanoparticles. Journal of Magnetism and Magnetic Materials. 2019;**488**:165378

[17] Younis M, Saleem M, Atiq S, Naseem S. Magnetic phase transition and magneto-dielectric analysis of spinel chromites: MCr_2O_4 (M = Fe, Co and Ni). Ceramics International. 2018;**44**:10229-10235

[18] Manjunatha K, Srininivasamurthy KM, Naveen CS, Ravikiran YT, Sitalo EI, Kubrin SP, et al. Observation of enhanced humidity sensing performance and structure, dielectric, optical and DC conductivity studies of scandium doped cobalt chromate. Journal of Materials Science: Materials in Electronics. 2019;**30**:17202-17217

[19] Manjunatha K, Jagadeesha Angadi V, Srinivasamurthy KM, Matteppanavar S, Pattar VK, Pasha UM. Exploring the structural, dielectric and magnetic properties of 5 Mol% Bi^{3+}-substituted $CoCr_2O_4$ nanoparticles. Journal of Superconductivity and Novel Magnetism. 2020;**71**:1-12

[20] Sathisha IC, Manjunatha K, Jagadeesha Angadi V, Chethan B, Ravikiran YT, Vinayaka K. et al. Enhanced humidity sensing response in Eu^{3+}-doped iron-rich Fe_2O_4: A detailed study of structural, microstructural, sensing, and dielectric properties. IntechOpen [Online First]; 2020. DOI: 10.5772/intechopen.90880.

[21] Koops CG. On the dispersion of resistivity and dielectric constant of some semiconductors at audio frequencies. Physical Review. 1951;**83**:121-124

[22] Jagdeesha Angadi V, Choudhury L, Sadhana K, Liu H-L, Sandhya R, Matteppanavar S, et al. Structural, electrical and magnetic properties of Sc^{3+} doped Mn-Zn ferrite nanoparticles. Journal of Magnetism and Magnetic Materials. 2017;**424**:1-11

[23] Jagadeesha Angadi V, Rudraswamy B, Sadhana K, Ramana Murthy S, Praveena K. Effect of Sm^{3+} - Gd^{3+} on structural, electrical and magnetic properties of MneZn ferrites synthesized via combustion route. Journal of Alloys and Compounds. 2016;**656**:5-12

[24] Kakade SG, Kambale RC, Kolekar YD, Ramana CV. Dielectric, electrical transport and magnetic properties of Er^{3+} substituted nanocrystalline cobalt ferrite. Journal of Physics and Chemistry of Solids. 2016;**98**:20-27

[25] Mangalaraja RV, Ananthakumar S, Manohar P, Gnanam FD. Magnetic, electrical and dielectric behaviour of $Ni_{0.8}Zn_{0.2}Fe_2O_4$ prepared through flash combustion technique. Journal of Magnetism and Magnetic Materials. 2002;**253**:56

[26] Tsay C-Y, Lin Y-H, Wang Y-M, Chang H-Y, Lei C-M, Jen S-U. Electrical transport properties of $CoMn_{0.2-x}GaxFe_{1.8}O_4$ ferrites using complex impedance spectroscopy. AIP Advances. 2016;**6**:055909

[27] Badapanda T, Sarangi S, Parida S, Behera B, Ojha B, Anwar S. Frequency and temperature dependence dielectric study of strontium modified barium zirconium titanate ceramics obtained by mechanochemical synthesis. Journal of Materials Science: Materials in Electronics. 2015;**26**:3069

[28] Sakthisabarimoorthi A, Dhas SAMB, Robert R, Influence

of erbium doping on the electrical behaviour of $CaCu_3Ti_4O_{12}$ ceramics probed by impedance spectroscopy analysis. Jose M. Materials Research Bulletin. 2018;**106**:81-92

[29] Manjunatha K, Jagadeesha Angadi V, Ribeiro RAP, Longo E, Oliveira MC, Bomio MRD, et al. Structural, electronic, vibrational and magnetic properties of Zn^{2+} substituted $MnCr_2O_4$ nanoparticles. Journal of Magnetism and Magnetic Materials. 2020;**502**:166595

[30] JagadeeshaAngadi V, Rudraswamy B, Sadhana K, Praveena K. Structural and magnetic properties of manganese zinc ferrite nanoparticles prepared by solution combustion method using mixture of fuels. Journal of Magnetism and Magnetic Materials. 2016;**409**:111-115